Supporting Information

Sharply Expanding Single-Atomically Dispersed Fe-N Active Sites through Bidirectional Coordination for Oxygen Reduction

Huihui Jin,[1,a,b,d] Ruohan Yu,[1,c] Pengxia Ji,[c] Weihao Zeng,[c] Zhengying Li,*[a,b,c] Daping He*[d] and Shichun Mu*[c]

[a] National Engineering Laboratory for Fiber Optic Sensing Technology, Wuhan University of Technology, Wuhan 430070, China

[b] School of Information Engineering, Wuhan University of Technology, Wuhan 430070, China

[c] State Key Laboratory of Advanced Technology for Materials Synthesis and Processing, Wuhan University of Technology, Wuhan 430070, China

[d] Hubei Engineering Research Center of RF-Microwave Technology and Application, School of Science, Wuhan University of Technology, Wuhan 430070, China

*Corresponding author.

E-mail: msc@whut.edu.cn, zhyli@whut.edu.cn, hedaping@whut.edu.cn

[1]These authors contributed equally

1 Experimental Section

1.1 Materials

The 2-methylimidazole (98%) used in the experiment was purchased from Aladdin, the commercial 20% Pt/C was purchased from JM Company, and other chemical reagents (analytical grade) were purchased from Sinopharm Chemical Reagent Co., Ltd. All chemical reagents were used directly without further purification. The resistivity of the deionized water used in the experiment was 18.25 MΩ*cm.

1.2 Morphology and Structure Characterization

Scanning electron microscopy (SEM, Zeiss Ultra Plus) and double spherical aberration-corrected transmission electron microscopy (ac-STEM-HAADF, Titan Cubed Themis G2 300) were used to collect the morphology information of the materials. Specific surface area and porosity analyzer (BET/BJH, ASAP 2020M), X-ray diffraction (XRD, D/Max-RB, using Cu Kα radiation at 12 kW, scan rate 5 o min-1), Raman spectroscopy (Raman, Renishaw Invia, using an incident laser at a wavelength of 633 nm), X-ray photoelectron spectroscopy (XPS, ESCALAB 250Xi) and Mössbauer spectroscopy to collect structural information on the material.

1.3 Electrochemical Calculations

In RDE testing, the electron transfer number was calculated by Koutecky-Levich equation:

$$\frac{1}{j} = \frac{1}{j_L} + \frac{1}{j_K} = \frac{1}{B\omega^{1/2}} + \frac{1}{j_K}$$

$$B = 0.62nFC_0D^{2/3}v^{-1/6}$$

Where j is the measured current density, j_K is the kinetic current density, j_L is the

limiting current density, ω is the angular velocity of the electrode rotation, n is the

electron transfer number, F is the Faraday constant (96485 C mol^{-1}), C_0 is the bulk

concentration of O_2 (1.2 $\times$ 10^{-6} mol cm^{-3} for 0.1 M KOH, 1.1 $\times$ 10^{-6} mol cm^{-3} for 0.5

M H_2SO_4), D is the diffusion coefficient of O_2 (1.9 $\times$ 10^{-5} cm^2 s^{-1} in 0.1 M KOH, 1.8

$\times$ 10^{-5} cm^2 s^{-1} in 0.5 M H_2SO_4), and ν is the kinematic viscosity of the electrolyte

(0.01 cm^2 s^{-1} for both 0.1 M KOH and 0.5 M H_2SO_4 solution).

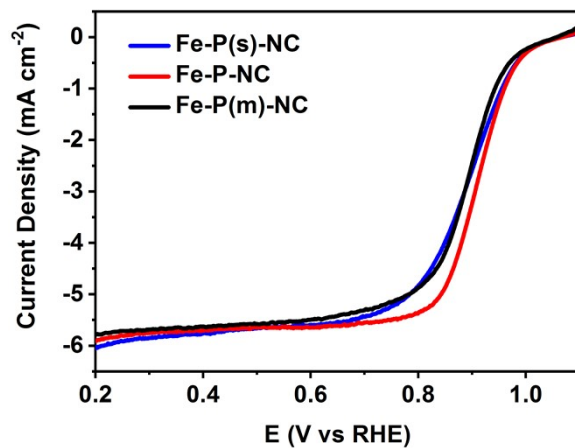**2 Supplementary Figures and Tables**

Fig. S1 LSV curves of products obtained with different amounts of triphenylphosphorus in 0.1 M KOH
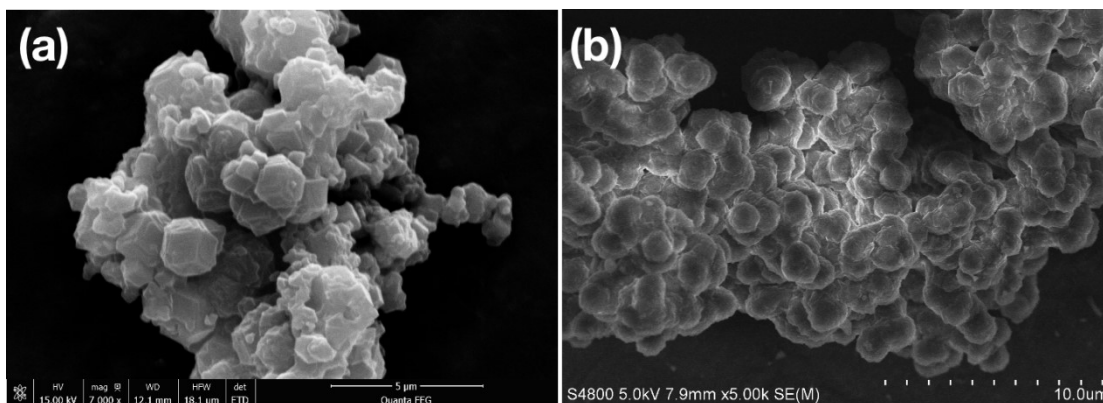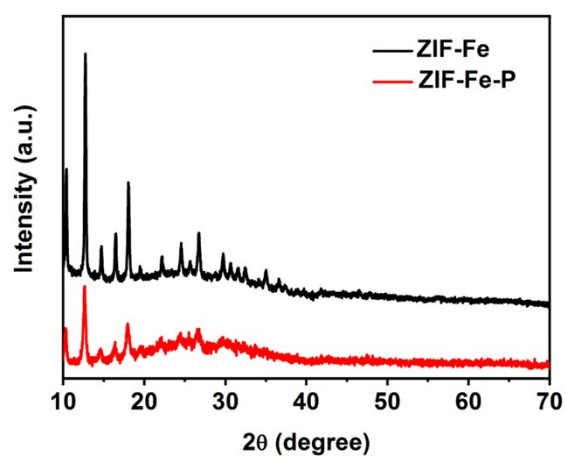

Fig. S2 SEM of (a) ZIF-Fe and ZIF-Fe-P

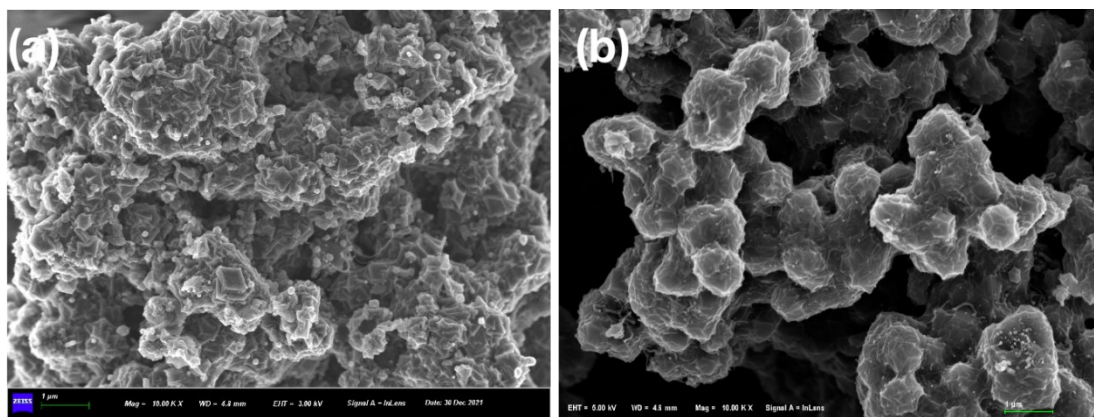**Fig. S3** XRD patterns of ZIF-Fe and ZIF-Fe-P

Fig. S4 SEM of (a) Fe-NC and Fe-P-NC
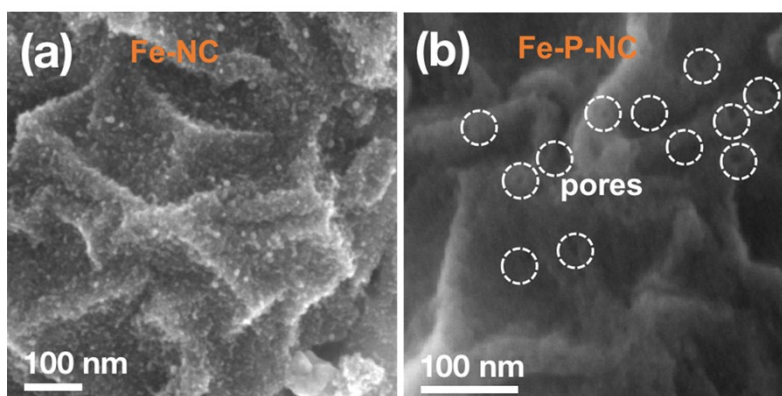

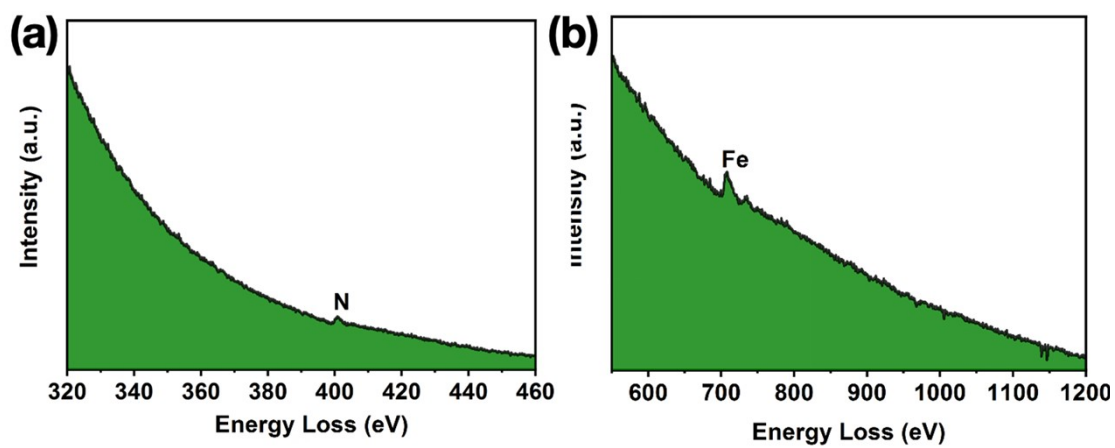**Fig. S5** SEM of Fe-NC and Fe-P-NC
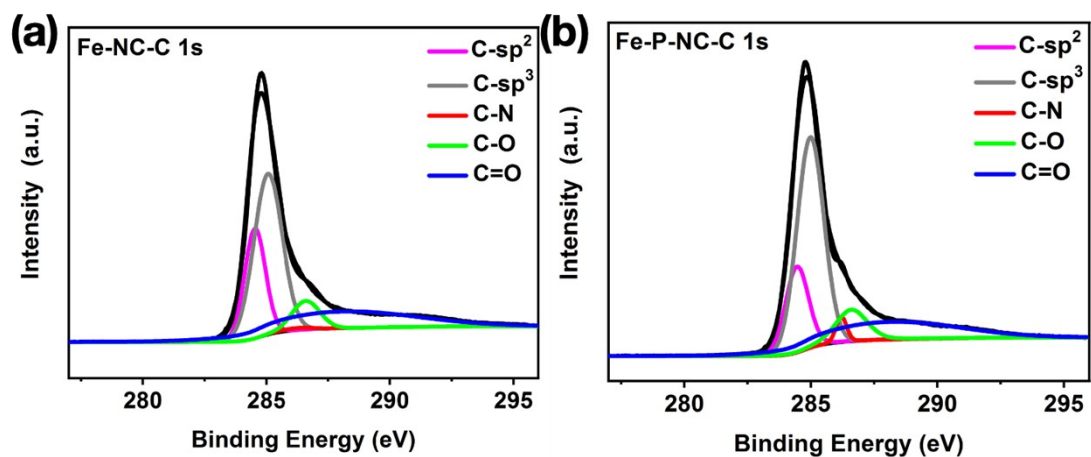

Fig. S6 EELS analysis of Fe-P-NC

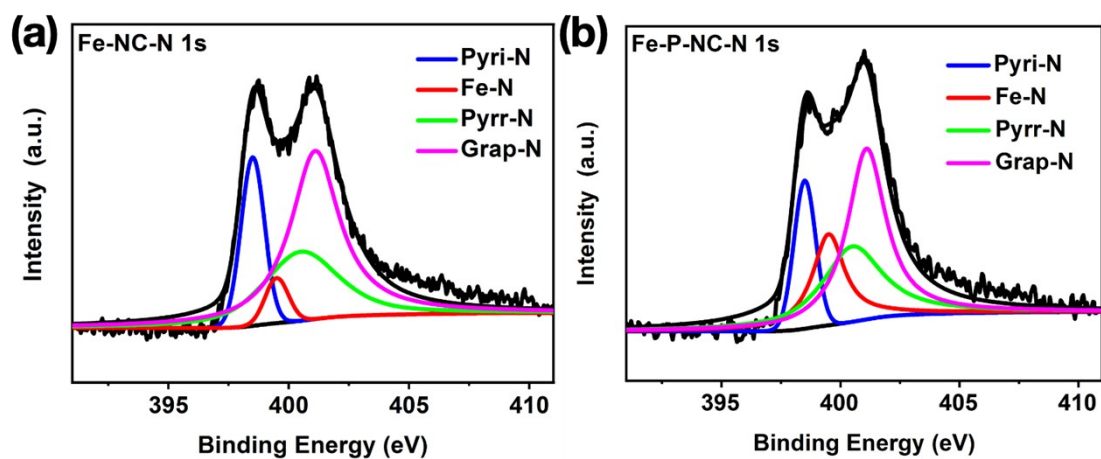**Fig. S7** C 1s XPS spectra of (a) Fe-NC and (b) Fe-P-NC

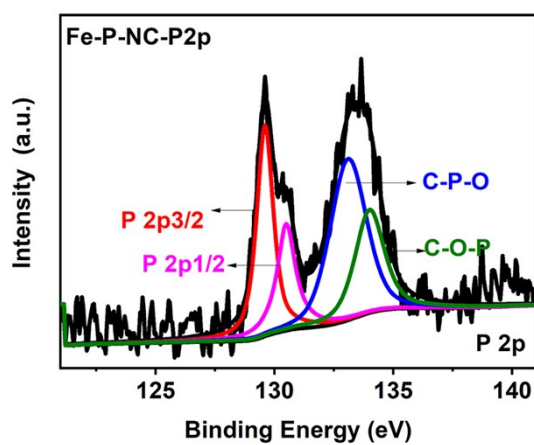**Fig. S8** N1s XPS spectra of (a) Fe-NC and (b) Fe-P-NC

Fig. S9 P2p XPS spectra Fe-P-NC
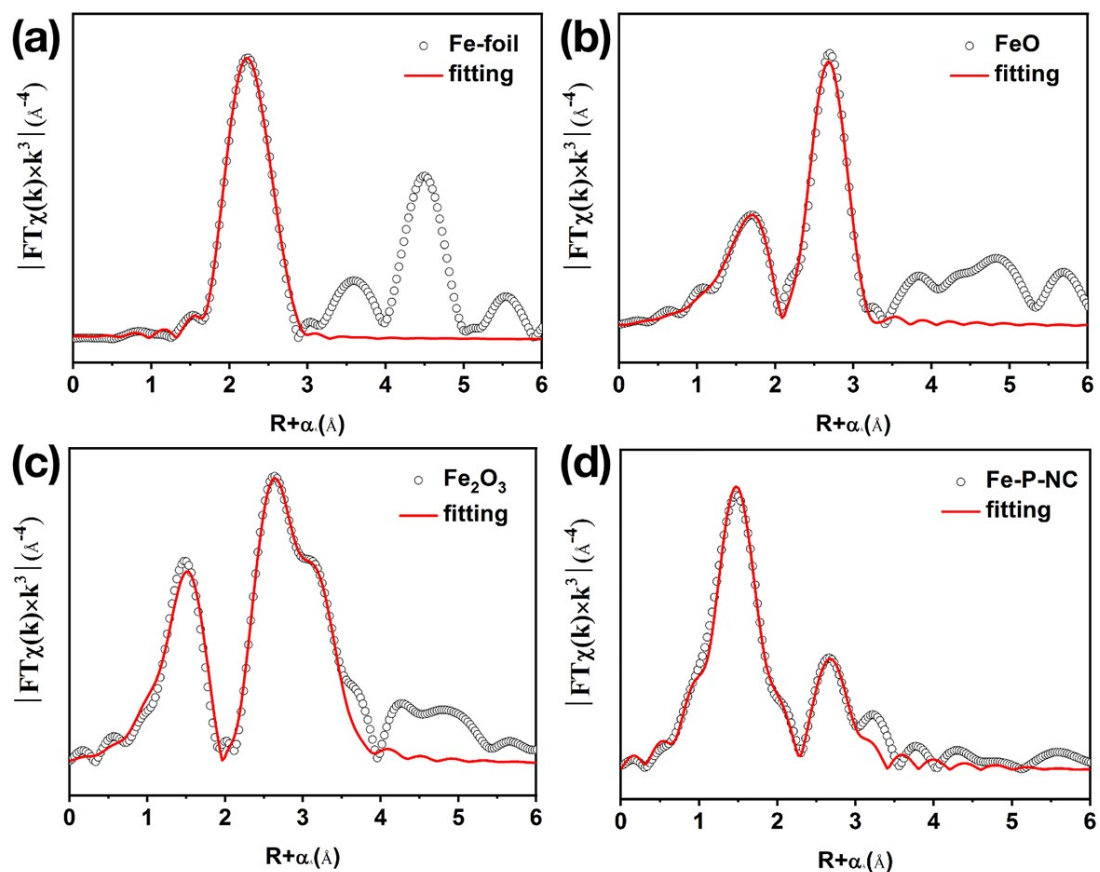
Fig. S10 Fitting results of EXAFS in R-space for Fe K-edge (a) Fe-foil, (b) FeO, (c) Fe_2O_3 and (d) Fe-P-NC
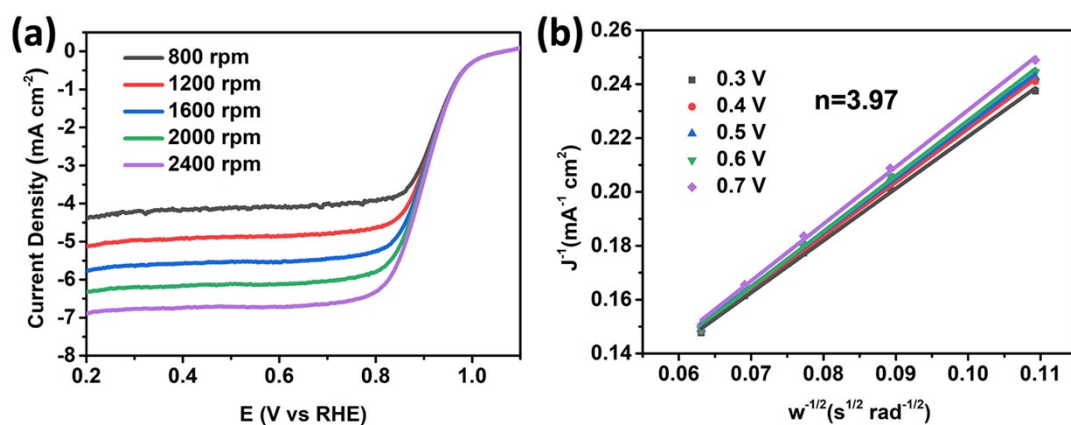
Fig. S11 (a) LSV curves at different rotational speeds and (b) linear K-L plots of Fe-P-NC under 0.1 M KOH
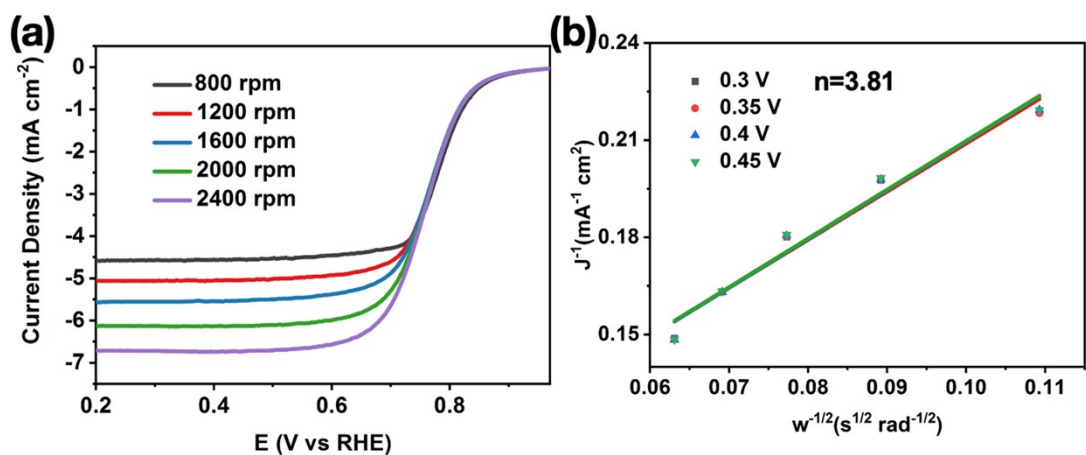
Fig. S12 (a) LSV curves at different rotational speeds and (b) linear K-L plots of Fe-P-NC under 0.5 M H_2SO_4
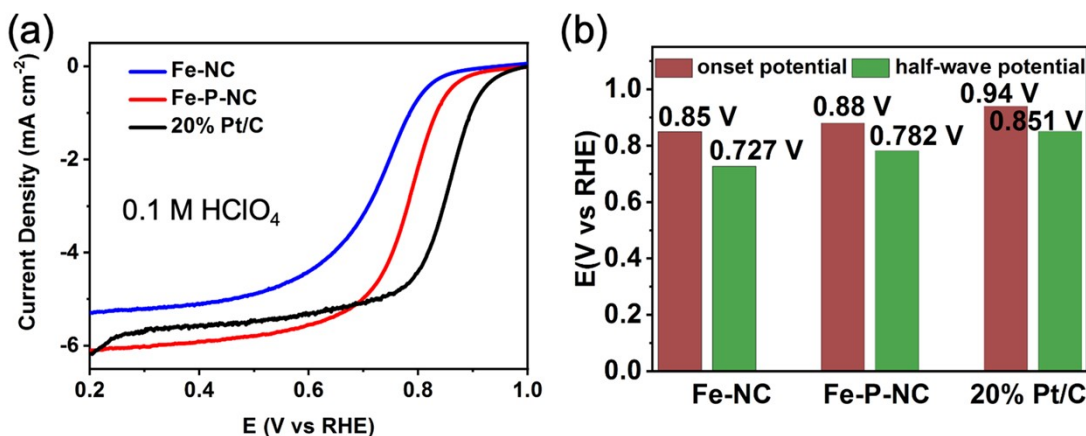
Fig. S13 (a) LSV curves and (b) comparison of onset potential and half-wave potential under 0.1 M $HClO_4$
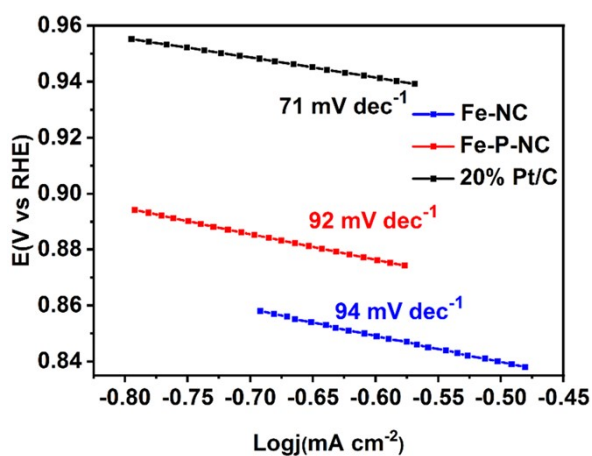
Fig. S14 Tafel plots of Fe-NC, Fe-P-NC and 20% Pt/C under 0.1 M $HClO_4$
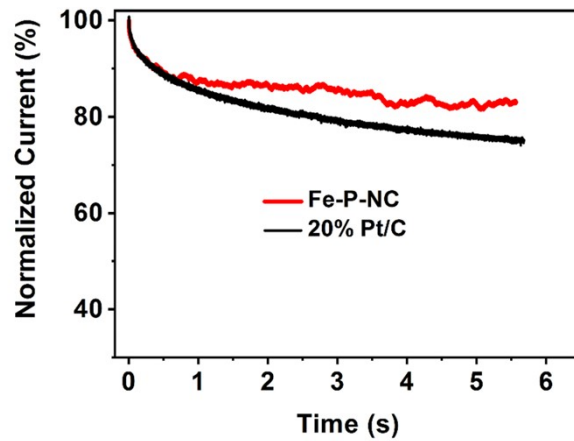
Fig. S15 Chronoamperometric response test of Fe-P-NC and 20% Pt/C under 0.1 M HClO$_4$
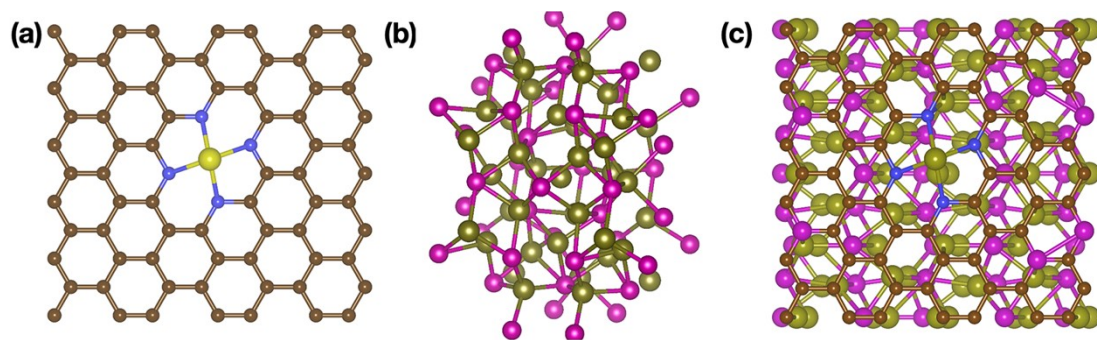
Fig. S16 Constructed computational model of (a) Fe-N$_4$, (b) Fe$_2$P and (c) Fe-N$_4$/Fe$_2$P
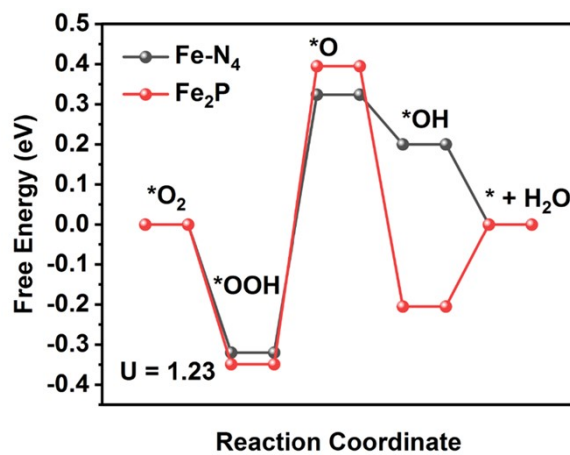
Fig. S17 ORR free energy path diagram of Fe-N$_4$ and Fe$_2$P

9
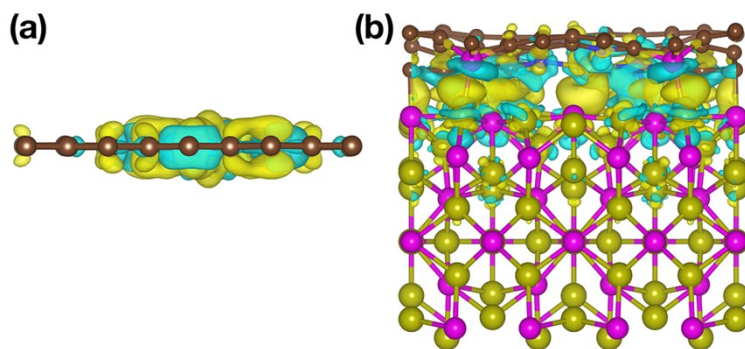
Fig. S18 Side view differential charge density of (a) Fe-N$_4$ and (b) Fe-N$_4$/Fe$_2$P
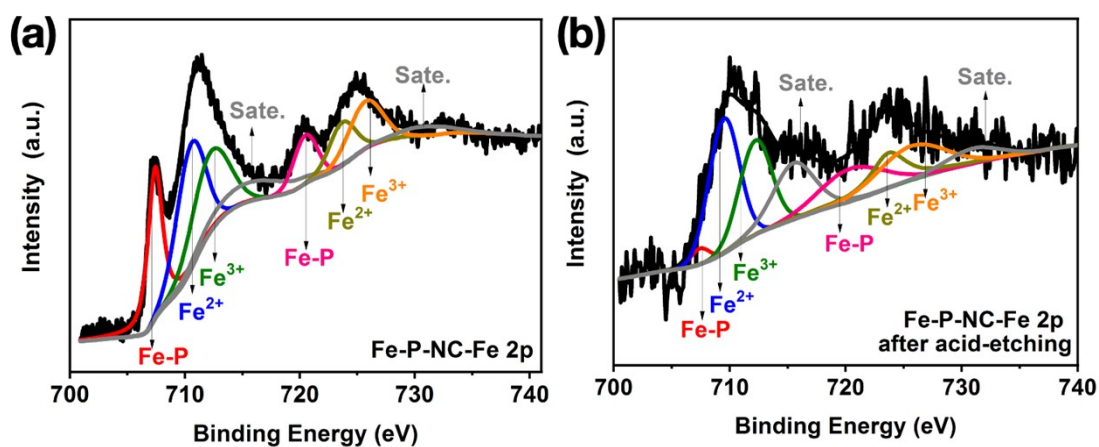
Fig. S19 Fe 2p XPS spectra of (a) Fe-P-NC and (b) Fe-P-NC after acid-etching
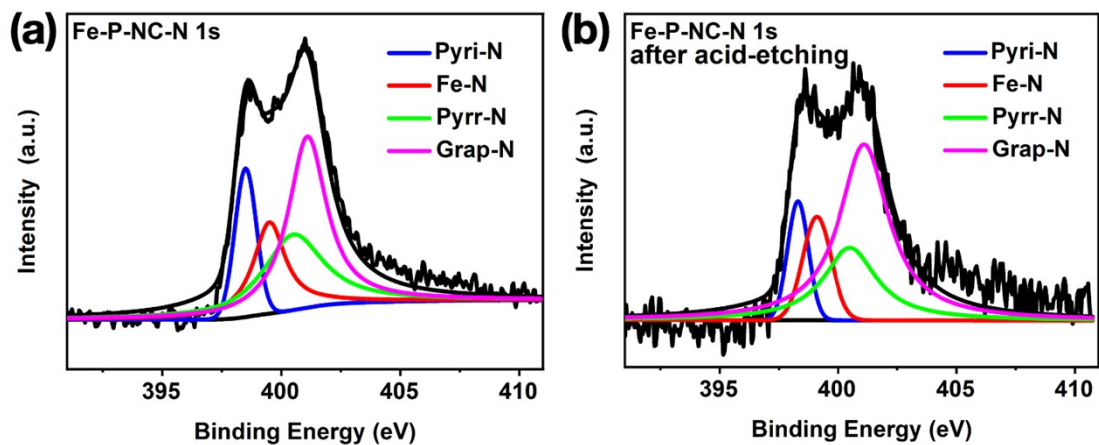
Fig. S20 N 1s XPS spectra of (a) Fe-P-NC and (b) Fe-P-NC after acid-etching
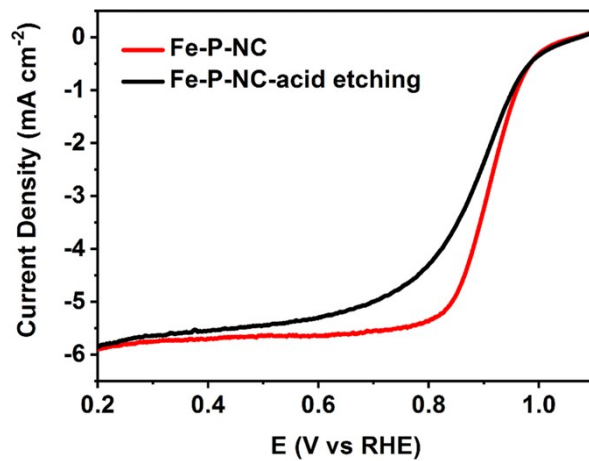
Fig. S21 LSV curves of Fe-P-NC before and after acid-etching in 0.1 M KOH

Table S1 The atomic contents from XPS results of N and Fe in Fe-NC and Fe-P-NC

Element content⟍sample	Fe (at.%)	N (at.%)	P (at.%)
Fe-NC	1.44 at.%	4.85 at.%	---
Fe-P-NC	1.79 at.%	6.62 at.%	1.06 at.%
Fe-P-NC (after acid-etching)	1.36 at.%	5.44 at.%	0.57 at.%

Table S2 EXAFS fitting parameters at the Fe K-edge for various samples

Sample	Shell	CN^a	$R(Å)^b$	$\sigma^2(Å^2)^c$	$\Delta E_0(eV)^d$	R factor
Fe-foil	Fe-Fe	8*	2.461±0.017	0.0049	4.5	0.0052
	Fe-Fe	6*	2.841±0.020	0.0045	3.7	
FeO	Fe-O	4.1±0.2	2.143±0.005	0.0129	6.6	0.0082
	Fe-Fe	9.1±0.3	3.063±0.003	0.0123	1.8	
Fe$_2$O$_3$	Fe-O	6.0±0.2	1.982±0.004	0.0108	-1.7	0.0045
	Fe-Fe	8.7±0.3	2.990±0.003	0.0106	3.4	
	Fe-Fe	4.8±0.3	3.648±0.005	0.0043	-10.6	
Fe-P-NC	Fe-N	4.4±0.2	1.977±0.003	0.0080	-3.7	0.0032
	Fe-P	0.9±0.1	2.340±0.011			
	Fe-Fe	0.8±0.1	3.060±0.010	0.0049	6.3	

Table S3 The fitted Mössbauer parameter table and the corresponding assignment of Fe-NC and Fe-P-NC. The isomer shift (IS), quadrupole splitting (QS), hyperfine field (H) and the relative content of each substance are given.

Sample	Component	IS (mm/s)	QS (mm/s)	H (kOe)	Area (%)	Assignments (Iron Phase)
Fe-NC	Singlet Site 1	0	0		9.7(43)	γ-Fe
	Doublet Site 1	0.310(63)	1.90(13)		2.8(31)	$Fe(III)-N_4$
	Doublet Site 2	0.290(39)	0.436(69)		33.3(71)	$Fe_{2+x}N$
	Sextet Site 1	0.279(68)	0.013(68)	491.5(46)	18.7(72)	Fe_2O_3
	Sextet Site 2	0.104(77)	0.091(77)	340.8(47)	4.9(37)	α-Fe
	Sextet Site 3	0.195(72)	0.015(67)	205.2(51)	22.0(88)	Fe_3C
	Sextet Site 4	0.33(11)	0.012(100)	159.9(71)	8.6(77)	Fe_3C
Fe-P-NC	Doublet Site 1	0.408(35)	0.776(56)		65.3(61)	$Fe(III)-N_4$
	Doublet Site 2	0.49(20)	3.41(38)		34.7(71)	$Fe_2P-Fe(II)$

Table S4. Comparison of half-wave potentials for ORR of iron-based catalysts from literature and this work in alkaline media

Catalyst	Electrolyte	$E_{1/2}$ vs RHE	Reference
P/Fe-N-C	0.1 M KOH	0.90 V	(1)
Fe-SA/PNC	0.1 M KOH	0.92 V	(2)
FePNC	0.1 M KOH	0.90 V	(3)
Fe-SA/PNC	0.1 M KOH	0.90 V	(4)
Fe-SA-PNC	0.1 M KOH	0.838 V	(5)
Fe,Co/DSA-NSC	0.1 M KOH	0.879 V	(6)
Fe SA/NCZ	0.1 M KOH	0.87 V	(7)
Fe-N,O/G	0.1 M KOH	0.86 V	(8)
Fe/Meso-NC-1000	0.1 M KOH	0.885 V	(9)
4.2-FeSA	0.1 M KOH	0.901 V	(10)
Fe-N-GDY	0.1 M KOH	0.89 V	(11)
Fe-P-NC	0.1 M KOH	0.906 V	This work

Table S5. Comparison of half-wave potentials for ORR of iron-based catalysts from literature and this work in acidic media

Catalyst	Electrolyte	$E_{1/2}$ vs RHE	Reference
Fe-SA/PNC	0.5 M H_2SO_4	0.86 V	(2)
Fe-NCs	0.5 M H_2SO_4	0.83 V	(12)
FePNC	0.5 M H_2SO_4	0.76 V	(3)
FeMn$_{ac}$/Mn-N$_4$C	0.5 M H_2SO_4	0.79 V	(13)
FeSNC	0.5 M H_2SO_4	0.76 V	(14)
Fe SAs-Fe$_2$P NPs/NPCFs-2.5	0.5 M H_2SO_4	0.78 V	(15)
Fe-KJB-3-60A	0.1 M $HClO_4$	0.79 V	(16)
4.2-FeSA	0.5 M H_2SO_4	0.74 V	(10)
Fe-Zn-SA/NC	0.1 M $HClO_4$	0.78 V	(17)
RN350-Z(1-2)-1000	0.1 M $HClO_4$	0.723 V	(18)
Fe-P-NC	0.1 M $HClO_4$	0.781 V	This work
	0.5 M H_2SO_4	0.779 V	

References

[1] Y. Zhou, R. Lu, X. Tao, Z. Qiu, G. Chen, J. Yang, Y. Zhao, X. Feng, K. Müllen, Boosting oxygen electrocatalytic activity of Fe-N-C catalysts by phosphorus incorporation, *J. Am. Chem. Soc.,* 2023, **145**, 3647-3655.

[2] W. Xue, Q. Zhou, X. Cui, J. Zhang, S. Zuo, F. Mo, J. Jiang, X. Zhu, Z. Lin, Atomically dispersed FeN_2P_2 motif with high activity and stability for oxygen reduction reaction over the entire pH range, *Angew. Chem. Int. Ed.,* 2023, **62**, e202307504.

[3] H. Liu, L. Jiang, Y. Sun, J. Khan, B. Feng, J. Xiao,H. Zhang, H. Xie, L. Li, S. Wang, L. Han, Asymmetric N, P-coordinated single-atomic Fe sites with Fe_2P nanoclusters/nanoparticles on porous carbon nanosheets for highly efficient oxygen electroreduction, *Adv. Energy Mater.,* 2023, **13**, 2301223.

[4] X. Yao, Y. Zhu, Z. Han, L. Yang, J. Tian, T. Xia, H. Peng, C. Cao, Solvent-mediated oxidative polymerization to atomically dispersed iron sites for oxygen reduction, *Appl. Catal. B:Environ.,* 2023, **331**, 122675.

[5] R. Pang, H. Xia, J. Li, E. Wang, Template-assisted formation of atomically dispersed iron anchoring on nitrogen-doped porous carbon matrix for efficient oxygen reduction, *Nano Res.,* 2023, **16**, 4671-4677.

[6] G. Yasin, S. Ali, S. Ibraheem, A. Kumar, M. Tabish, M. A. Mushtaq, S. Ajmal, M. Arif, M. A. Khan, A. Saad, L. Qiao, W. Zhao, Simultaneously engineering the synergistic-effects and coordination-environment of dual-single-atomic iron/cobalt-sites as a bifunctional oxygen electrocatalyst for rechargeable zinc-air batteries, *ACS*

Catal., 2023, **13**, 2313-2325.

[7] C. Jiao, Z. Xu, J. Shao, Y. Xia, J. Tseng, G. Ren, N. Zhang, P. Liu, C. Liu, G. Li, S. Chen, S. Q. Chen, H. L. Wang, High-density atomic Fe-N$_4$/C in tubular, biomass-derived, nitrogen-rich porous carbon as air-Eelectrodes for flexible Zn-air batteries, *Adv. Funct. Mater.,* 2023, **33**, 2213897.

[8] Y. Li, Y. Ding, B. Zhang, Y. Huang, H. Qi, P. Das, L. Zhang, X. Wang, Z. S. Wu, X. Bao, N,O symmetric double coordination of an unsaturated Fe single-atom confined within a graphene framework for extraordinarily boosting oxygen reduction in Zn-air batteries, *Energy Environ. Sci.,* 2023, **16**, 2629-2636.

[9] S. N. Zhao, J. K. Li, R. Wang, J. Cai, S. Q. Zang, Electronically and geometrically modified single-atom Fe sites by adjacent Fe nanoparticles for enhanced oxygen reduction, *Adv. Mater.,* 2022, **34**, 2107291.

[10] X. Wu, Q. Wang, S. Yang, J. Zhang, Y. Cheng, H. Tang, L. Ma, X. Min, C. Tang, S. P. Jiang, F. Wu, Y. Lei, S. Ciampic, S. Wang, L. Dai, Sublayer-enhanced atomic sites of single atom catalysts through in situ atomization of metal oxide nanoparticles, *Energy Environ. Sci.,* 2022, **15**, 1183-1191.

[11] M. Li, Q. Lv, W. Si, Z. Hou, C. Huang, Sp-hybridized nitrogen as new anchoring sites of iron single atoms to boost the oxygen reduction reaction, *Angew. Chem. Int. Ed.,* 2022, **61**, e202208238.

[12] S. Y. Yi, E. Choi, H. Y. Jang, S. Lee, J. Park, D. Choi, Y. Jang, H. Kang, S. Back, S. Jang, J. Lee, Insight into defect engineering of atomically dispersed iron electrocatalysts for high-performance proton exchange membrane fuel cell, Adv.

Mater., 2023, 2302666.

[13] H. Liu, L. Jiang, J. Khan, X. Wang, J. Xiao, H. Zhang, H. Xie, L. Li, S. Wang, L. Han, Decorating single-atomic Mn sites with FeMn clusters to boost oxygen reduction reaction, *Angew. Chem. Int. Ed.,* 2023, **135**, e202214988.

[14] H. Liu, L. Jiang, Y. Sun, J. Khan, B. Feng, J. Xiao, H. Zhang, H. Xie, L. Li, S. Wang, L. Han, Revisiting the role of sulfur functionality in regulating the electron distribution of single-atomic Fe sites toward enhanced oxygen reduction, *Adv. Funct. Mater.,* 2023, **33**, 2304074.

[15] Y. Pan, X. Ma, M. Wang, X. Yang, S. Liu, H. Chen, Z. Zhuang, Y. Zhang, W. Cheong, C. Zhang, X. Cao, R. Shen, Q. Xu, W. Zhu, Y. Liu, X. Wang, X. Zhang, W. Yan, J. Li, H. Chen, C. Chen, Y. Li, Construction of N, P co-doped carbon frames anchored with Fe single atoms and Fe_2P nanoparticles as a robust coupling catalyst for electrocatalytic oxygen reduction, *Adv. Mater.,* 2022, **34**, 2203621.

[16] M. Wang, B. Huang, N. Jiang, T. Liu, J. Huang, L. Guan, An Fe-N-C electrocatalyst with dense active sites synthesized by expeditious pyrolysis of a natural $Fe-N_4$ macrocyclic complex, *J. Mater. Chem. A,* 2022, **10**, 23001-23007.

[17] J. Xu, S. Lai, D. Qi, M. Hu, X. Peng, Y. Liu, W. Liu, G. Hu, H. Xu, F. Li, C. Li, J. He, L. Zhuo, J. Sun, Y. Qiu, S. Zhang, J. Luo, X. Liu, Atomic Fe-Zn dual-metal sites for high-efficiency pH-universal oxygen reduction catalysis, *Nano Res.,* 2021, **14**, 1374-1381.

[18] M. Hao, R. Dun, Y. Su, L. He, F. Ning, X. Zhou, W. Li, In situ self-doped biomass-derived porous carbon as an excellent oxygen reduction electrocatalyst for

fuel cells and metal–air batteries, *J. Mater. Chem. A,* 2021, **9**, 14331-14343.